

1 **Measurement report: Vehicle-based ~~and In-Situ~~ Multi-**
2 **lidar Observational Study of ~~in~~ the Effect of Meteorological**
3 **Elements on the Three-dimensional Distribution of**
4 **Particles in the Western Guangdong–Hong Kong–Macao**
5 **Greater Bay Area**

6 Xinqi Xu^{1,2}, Jielan Xie^{1,2}, Yuman Li^{1,2}, Shengjie Miao^{1,2}, and Shaojia Fan^{1,2}

7 ¹School of Atmospheric Sciences, Sun Yat-sen University, Zhuhai, 519082, China

8 ²Guangdong Provincial Observation and Research Station for Climate Environment and Air Quality
9 Change in the Pearl River Estuary, Key Laboratory of Tropical Atmosphere–Ocean System, Ministry of
10 Education, Southern Marine Science and Engineering Guangdong Laboratory (Zhuhai), Zhuhai, 519082,
11 China

12 *Correspondence to:* Shaojia Fan (eesfsj@mail.sysu.edu.cn)

13 **Abstract:** The distribution of meteorological elements has always been an important factor in
14 determining the horizontal and vertical distribution of particles in the atmosphere. To study the effect
15 of meteorological elements on the three-dimensional distribution structure of particles, mobile vehicle
16 lidar ~~observations~~, and in-situ fixed-location observations ~~were were collected presented~~ in the western
17 Guangdong–Hong Kong–Macao Greater Bay Area of China during September and October ~~efin~~ 2019
18 and 2020. Vertical aerosol extinction coefficient, depolarization ratio, and wind and temperature
19 profiles were ~~measured by~~ using a micro pulse lidar, a Raman scattering lidar, and a Doppler wind
20 profile lidar installed on a mobile monitoring vehicle. The mechanism of how wind and temperature in
21 the boundary layer affects the horizontal and vertical distribution of particles was ~~analyzed~~. The
22 results ~~showed~~ that particles were mostly distributed in downstream areas on days with moderate wind
23 speed in the boundary layer, ~~while whereas~~ they ~~presented were distributed~~ homogeneously on days
24 with weaker wind. There are three typical types of vertical distribution of particles in the western
25 Guangdong–Hong Kong–Macao Greater Bay Area (GBA): surface single layer, elevated single layer,
26 and double layer. Analysis of wind profiles and Hybrid Single-Particle Lagrangian Integrated
27 Trajectory Model (HYSPLIT) backward trajectory ~~revealed~~ different sources of particles for the three
28 types. Particles ~~concentrating~~ near the temperature inversion and multiple inversions could cause
29 more than one peak in the extinction coefficient profile. There ~~were are~~ two mechanisms ~~that~~
30 ~~affecting~~ the distribution of particulate matter in the upper and lower boundary layers. Based on ~~this~~
31 observational study, a general model of meteorological elements affecting the vertical distribution of
32 urban particulate matter ~~was is made proposed~~.

33 **1. Introduction**

34 The Guangdong–Hong Kong–Macao Greater Bay Area (GBA) is one of China’s national key
35 economic development regions. It consists of Guangzhou (GZ), Shenzhen (SZ), Zhuhai (ZH), Foshan
36 (FS), Huizhou (HZ), Dongguan (DG), Zhongshan (ZS), Jiangmen (JM), and Zhaoqing (ZQ) in

37 Guangdong province, as well as Hong Kong and Macao, the two Special Administrative Regions.
38 Covering 56,000 square ~~kilometers~~kilometres, the GBA had a vast population of over 70 million at the
39 end of 2018. The GBA plays a significant role in boosting global trade along the land-based Silk Road
40 Economic Belt and the 21st Century Maritime Silk Road. With the rapid development of the regional
41 economy, increasingly more studies on air quality and climate effect in the GBA have also been
42 conducted (Fang et al., 2018; Shao et al., 2020; Zhou et al., 2018).

43
44 ~~Anthophogenie~~Anthropogenic particles in the air play an important role in the environment of human
45 living. They not only act as air pollutants posing harmful effects to human health (Liao et al., 2017;
46 Leikauf et al., 2020; Yao et al., 2020; Orru et al., 2017) but also alter the temperature near the ground
47 owing to their ability to absorb and scatter solar radiation (IPCC, 2014; Strawa et al., 2010). As a result
48 of ~~industrialization~~industrialisation and ~~urbanization~~urbanisation, megacity clusters in China such as
49 the Beijing–Tianjin–Hebei [also called Jing–Jin–Ji (JJJ) in Chinese] area, Yangtze River Delta (YRD),
50 and Guangdong–Hong Kong–Macao GBA, have been seriously affected by particulate matter in recent
51 years. Numerous studies on the particulate matter have been conducted in these areas (Xu et al., 2018;
52 Liu et al., 2017; Du et al., 2017). Particles in the boundary layer can, directly and indirectly, affect
53 human lives and activities. Therefore, it is essential to study their distribution characteristics.

54
55 The distribution of particles is influenced not only by changes in source emissions but also by changes
56 in meteorological factors, such as temperature and wind. ~~It has previously been observed that a low~~
57 ~~boundary layer height and complex vertical distributions of aerosols, temperature, and relative~~
58 ~~humidity are the main structural characteristics of haze days (Huige et al., 2021). For example,~~
59 ~~P~~revious studies have confirmed that different types of temperature inversions have different impacts
60 on particles in the boundary layer (Wallace et al., 2009; ~~Wang et al., 2018~~). ~~The depth and temperature~~
61 ~~difference of the inversion region is a key factor for predictions of surface PM_{2.5} concentrations~~; (Zang
62 et al., 2017). ~~It has been previously observed that wind fields play an important role in transboundary-~~
63 ~~local aerosol interactions (Huang et al., 2021a; Huang et al., 2021b). Recent evidence suggests that~~
64 ~~wind shear is an important factor in terms of PM₁₀ vertical profile modification (Sekula et al., 2021).~~
65 The concentration of particulate matter also shows characteristics of wind-dependent spatial
66 distributions in which pollutant transport within the GBA city cluster is significant (Xie et al., 2019).
67 Hence, the issue of how meteorological factors affecting the distribution of particles has received
68 considerable critical attention.

69
70 Lidar is an active remote sensing device. It emits a laser light beam and receives a backscatter signal,
71 which can be further used to retrieve ~~the~~ vertical distribution of particle optical properties, ~~as well as~~
72 ~~wind~~, and temperature. It has been ~~wildly~~widely applied in the fields of meteorology and
73 environmental science. In most ~~of the research~~studies, it ~~was~~is used as a ground-based or satellite-
74 based instrument (Tian et al., 2016; Liu et al., 2017; Heese et al., 2017).

75
76 In recent years, vehicle-based lidar observation has ~~been~~ gradually developed and become a powerful
77 tool to detect the physical and chemical properties of the boundary layer. Compared with ~~the~~ traditional
78 ~~in-situ~~ observations, it can carry out continuous mobile observations and obtain the change of ~~the~~
79 vertical profiles of certain factors in ~~the~~ its path. Additionally, ~~it can be used as~~ a mobile lidar system
80 ~~can be used~~ to conduct supplementary observations in areas with no lidar ~~assembled~~present. In the past

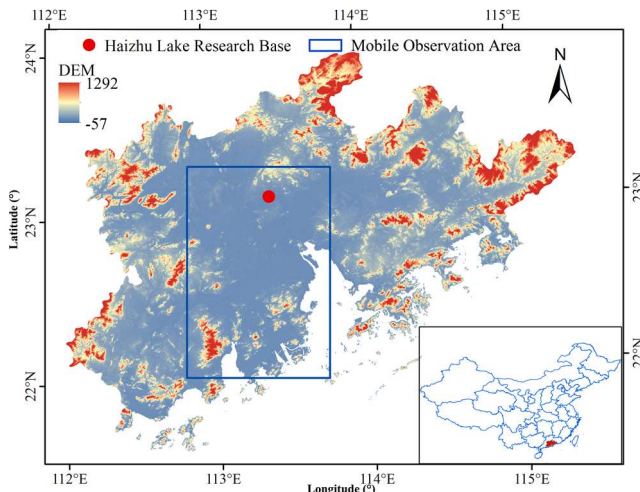
81 few years, several vehicle-based observational experiments have been carried out (Lv et al., 2017; Lyu
82 et al., 2018; Lv et al., 2020; Zhao et al., 2021; Fan et al., 2018), but research aimed at multi-lidar
83 observations and the effect of the vertical structure of meteorological factors onto the distribution of
84 particles hassd been a largely been an underexplored domain, especially in the GBA. The former
85 research revealed that pollution of particulate matter frequently occurs in the western part of inland
86 regions of GBA (Fang et al., 2019), affecting downstream cities under the northerly wind field. Hence,
87 the authors were motivated to perform observations in the western GBA with a multi-lidar system
88 installed on the a vehicle to study the influence of the three-dimensional structure of meteorological
89 elements on the distribution of particles.

90 **2. Data and Method**

91 **2.1 Description of Observations**

92 The horizontal distribution of the particles was studied by making mobile vehicle lidar observations
93 over the west bank of the Pearl River Estuary. During the mobile vehicle lidar observations experiment,
94 the vehicle drove was driven clockwise along the west bank of the Pearl River Estuary, passing through
95 main cities of the GBA in the route, from as far north as Guangzhou to as far south as Zhuhai. The total
96 length of the route was approximately 320 km, and the experiment was conducted during the daytime.
97 The vehicle-based observation lasted for seven continuous days, which started on 29 August 29th and
98 ended on 4 September 4th, 2020. During most of the mobile observations, the relative humidity of
99 Zhuhai, the closest city to the sea, was below 60 %. Therefore, the influence of hygroscopic growth on
100 the extinction coefficient was negligible. To study the vertical distribution of the particles, —in situ—
101 observations were made at Haizhu Lake Research Base in September and October of 2019 and 2020 we
102 conducted fixed-location lidar observation experiments using the same lidar system from September
103 10th to October 8th, 2019, and from August 29th to October 27th, 2020, totalling 89 days. The reason
104 for choosing these periods is that they include the wet season change to the dry season in the GBA area.
105 Therefore, changes in meteorological elements have a significant impact on the three-dimensional
106 distribution of particles. The location of the Haizhu Lake Research Base and the area of the measuring
107 path are shown in Fig. 1. The research area is on the Pearl River Delta Plain. This area is bordered by
108 the Nanling Mountains in the north. Mountain obstruction makes the GBA area less susceptible to
109 long-distance transport of pollutants from other areas, and the transport of pollutants mainly occurs
110 between cities in the research area. Observations with the vehicle-based multi-lidar system are listed in
111 Table 1.

112



113
114 **Figure 1. Location of the Haizhu Lake Research Base and area of the mobile observation path area.**
115
116

Table 1. Observations with the vehicle-based multi-lidar system

Time	Observation
Sept. 10th – Oct. 8th, 2019	Fixed-location observation
Aug. 29th – Sept. 4th, 2020, in the daytime	Mobile observation
Aug. 29th – Sept. 4th, 2020, at night	Fixed-location observation
Sept. 5th – Oct. 27th, 2020	Fixed-location observation

117
118 **2.2 Multi-lidar System**

119 A multi-lidar system was installed on a vehicle in this experiment. The car used was a modified 7-
120 seater Mercedes-Benz sport utility vehicle. Three lidars were fixed to the rear of the car by steel bars to
121 ensure their stability. To avoid the impact of frequent changes in speed and vehicle bumps during the
122 observation, the routes of mobile observations were basically flat highways, and the driving speed was
123 controlled within 80 km/h. During fixed-location observations, the car was parked in the observation
124 field and connected to a stable power source. The lidar system included a 3D visual scanning micro
125 pulse lidar (EV-Lidar-CAM, EVERISE Company, Beijing,
126 <http://www.everisetech.com.cn/products/ygtc/evlidarportable.html>), a twirling Raman temperature
127 profile lidar (TRL20, EVERISE Company, Beijing,
128 <http://www.everisetech.com.cn/products/ygtc/templidar.html>), a Doppler wind profile lidar
129 (Windview10, EVERISE Company, Beijing,
130 <http://www.everisetech.com.cn/products/ygtc/windview10.html>), a global positioning system (GPS),
131 and a signal acquisition unit. The three lidars are characterized characterised by high temporal and
132 spatial resolution, and can effectively identify determine the evolution of the vertical distribution of
133 particles, as well as temperature, wind speed, and wind direction over time. Remote sensing
134 observations, such as lidar, are generally considered to be less accurate than direct observations from
135 aircraft and meteorological tower-based sensors. Therefore, the quality of data from the lidar system
136 was checked before using in our study. Results show that the percentage difference between data
137 provided by the lidar system and data from the Shenzhen meteorological tower was less than 15%,
138 which indicates a sufficient accuracy of the lidar instrument. We have used this lidar system in our

139 previous research and showed it to be reliable (He et al., 2021a; He et al., 2021b). The vehicle setup is
 140 shown in Figure 2. The details of the three lidars are shown in Table 42.



142
 143 **Figure 2. Setup of the multi-lidar system on the vehicle.**

144
 145 **Table 42.: Detailed parameters for the three lidars.**

Lidar	Variable	Laser source	Wave length	Laser frequency	Spatial resolution	Time resolution
Micro pulse lidar	Original signal, Extinction coefficient profiles, Depolarization ratio profiles, Aerosol optical depth	Nd:YAG laser	532 nm	2500 Hz	15 m	1 min
Raman temperature profile lidar	Temperature profiles	Nd:YAG laser	532 nm	20 Hz	60 m	5 min
Doppler wind profile lidar	Wind speed profiles, Wind direction profiles	Fiber	1545 nm	10 kHz	50 m	1 min

146

147 2.3 Calculation of Extinction Coefficient and Depolarization Ratio

148 The aerosol extinction coefficient represents the reduction of radiation in a band owing to scattering
 149 and absorption by aerosols (Li et al., 2020). The formula for the extinction coefficient calculation
 150 (Fernald, 1984) is as follows:

$$151 \quad \alpha_a(z) = -\frac{S_a}{S_m} \alpha_m(z) + \frac{P(z)z^2 \cdot \exp[2\left(\frac{S_a}{S_m}-1\right) \int_z^{z_c} \alpha_m(z) dz]}{\frac{P(z_c)z^2}{\alpha_a(z_c) + \frac{S_a}{S_m} \alpha_m(z_c)} + 2 \int_z^{z_c} P(z)z^2 \exp[2\left(\frac{S_a}{S_m}-1\right) \int_z^{z_c} \alpha_m(z) dz] dz} \quad (1)$$

153
 154 where $P(z)$ is the power received at altitude z , α_a and α_m denote the particle extinction and
 155 molecular extinction, respectively and $S_a = 50 \text{ Sr}$ is the particle extinction-to-backscatter ratio.

156 which is the default value given by the manufacturer. This value is consistent with prior work in the
157 GBA area (Li et al., 2020). $S_m = 8\pi/3$ is the molecular extinction-to-backscatter ratio, and z_c is the
158 calibration height of the micro pulse lidar, which is variable, ranging from 10-15 km, and depending on
159 the signal intensity.

160
161 The micro pulse lidar (MPL) system uses the scattering of polarized light to distinguish between
162 spherical and non-spherical particles to ascertain the particle species (Li et al., 2020). The
163 depolarization ratio is calculated with the following formula:

164

$$\delta = k \frac{P_{\perp}}{P_{\parallel}} \quad (2)$$

165
166 where P_{\perp} and P_{\parallel} represent the cross-polarized and co-polarized signal, respectively. k the
167 depolarization calibration constant, which is the ratio of the gains of the parallel and perpendicular
168 channels (Dai et al., 2018).

170 2.4 HYSPLIT Backward Trajectory Model

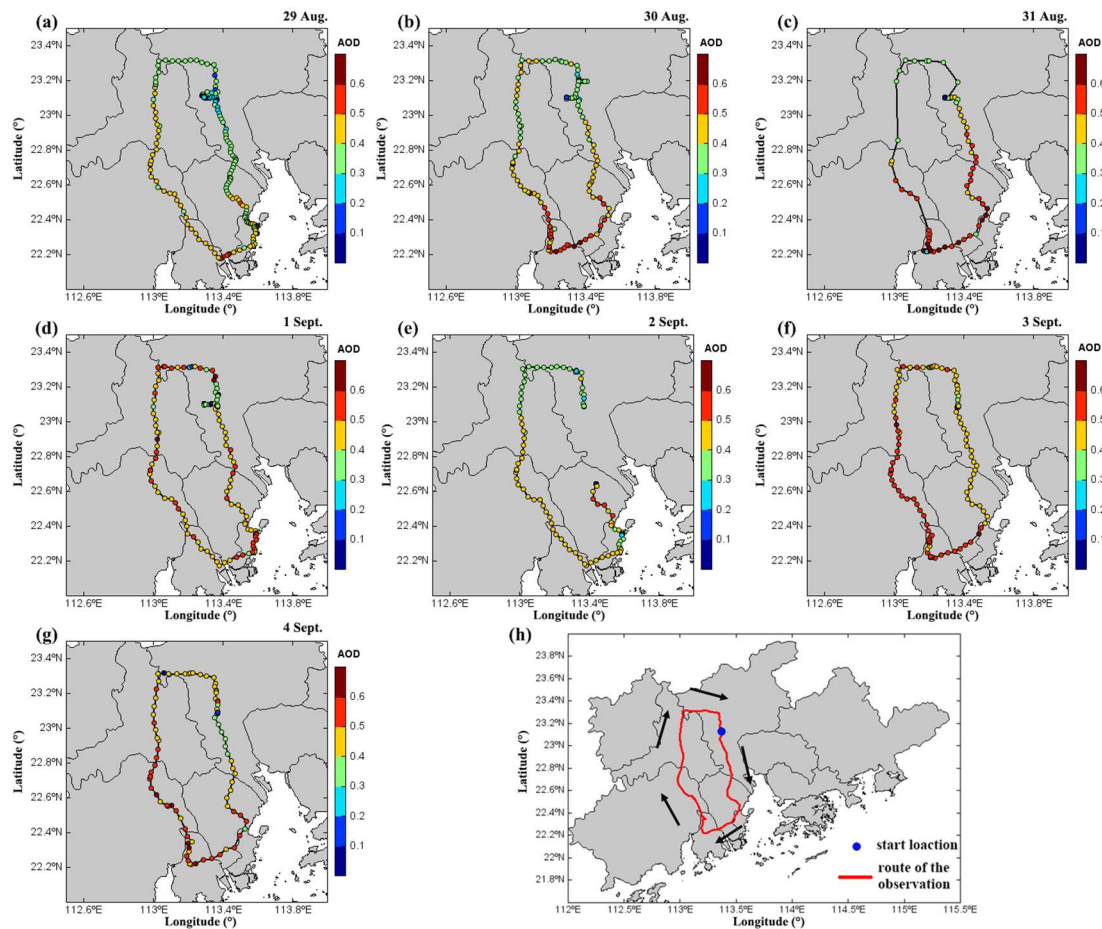
171 The regional transport of particulate matter was studied using the National Oceanic and Atmospheric
172 Administration Hybrid Single-Particle Lagrangian Integrated Trajectory Model (HYSPLIT) so as to
173 determine the trajectory of air masses. It has been widely used in the field of air masses and pollutant
174 source analysis (Deng et al., 2016; Lu et al., 2018; Kim et al., 2020). In this study, meteorological data
175 of the Global Data Assimilation System (GDAS) at the spatial resolution of 0.25° was used. To obtain
176 the sources of particulate matter at different heights, altitudes of 100 m, 500 m, and 1000 m were set as
177 the ending points of the trajectories.

178 3. Results and Discussion

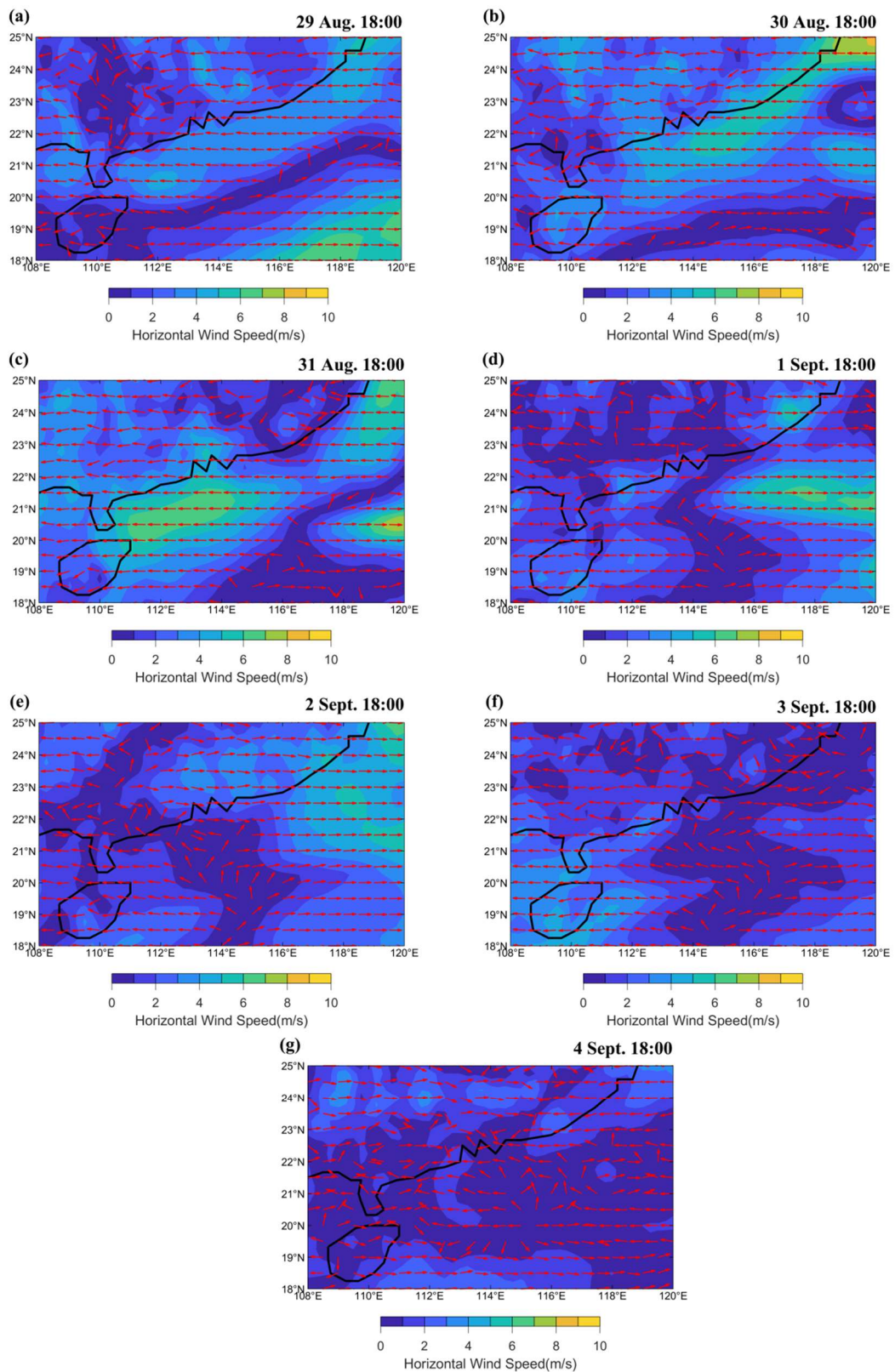
179 3.1 Mobile Vehicle Lidar Observations

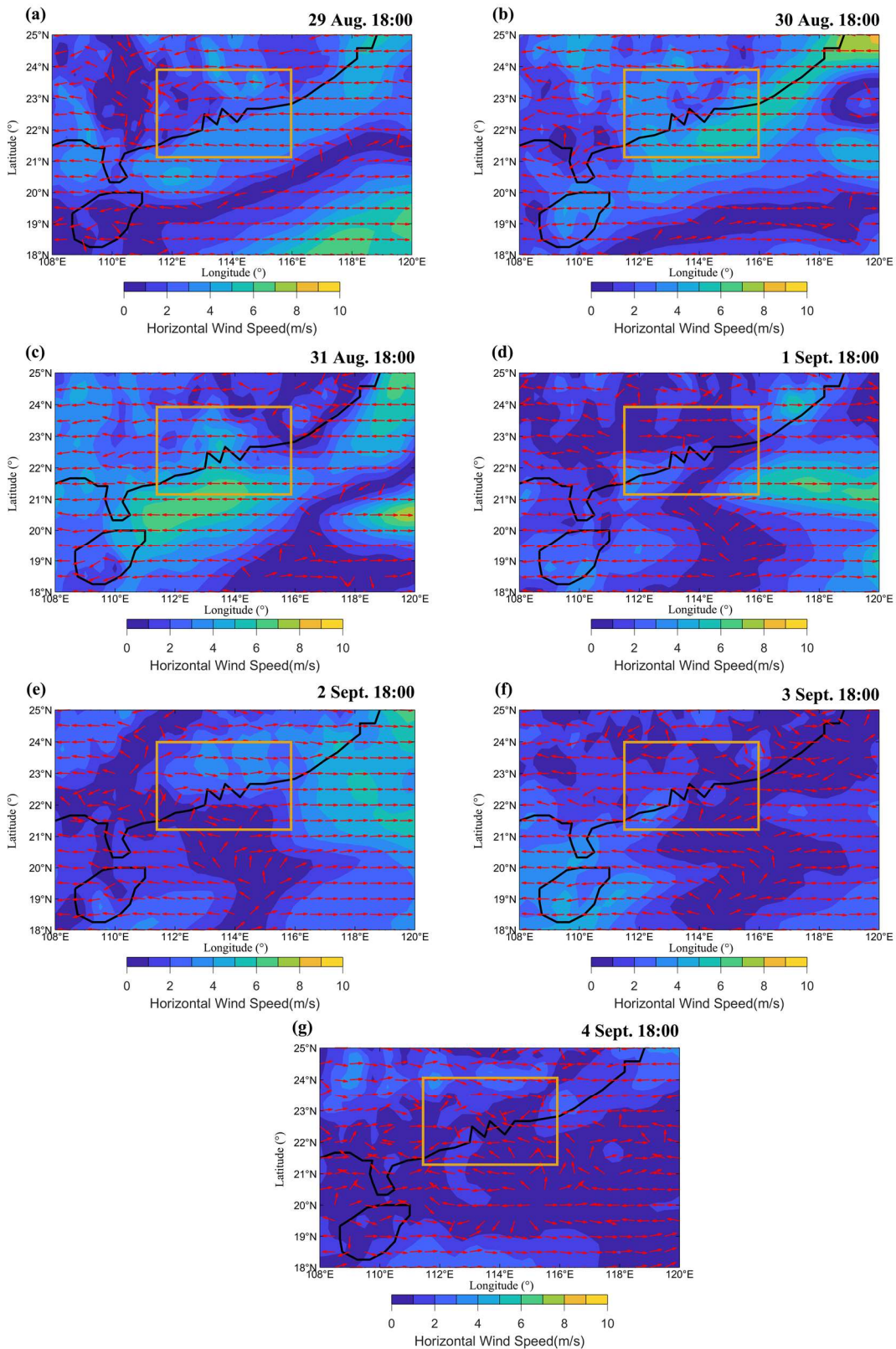
180 The horizontal distribution of particles was obtained by conducting mobile vehicle lidar observations in
181 the GBA. The reason for choosing this route is that it covers the major urban agglomerations in the
182 western part of the Guangdong–Hong Kong–Macao Greater Bay Area, which contains a large number
183 of anthropogenic aerosol emission sources. It is representative of the regional distribution of particles
184 in this area. We conducted mobile observations once a day, from August 29th to September 4th, 2020.
185 The set off time was at 10:00 and a single measurement circle was completed at around 16:00. Owing
186 to surface heating, convection in the boundary layer develops vigorously during daytime, which allows
187 aerosols to mix well and form a more homogeneous vertical distribution. Therefore, mobile
188 observations during the daytime are more appropriate to study the horizontal distribution of particles in
189 the GBA area. Figure 2-3 shows the aerosol optical depth (AOD) measured with the MPL in the route.
190 Because of GPS signal interference, some GPS data on 31-August 31st and 2-September 2nd were
191 missing. On most days, sections with high AOD values fell geographically into the south and west
192 sides of the observation region. Figure 3-4 demonstrates shows low-level horizontal wind fields on 925
193 hPa over the region based on ERA5 reanalysis data
194 (<https://cds.climate.copernicus.eu/cdsapp#!/dataset/reanalysis-era5-pressure-levels?tab=overview>). In

195 the first three days, the wind speed over the GBA was generally higher, and the wind direction was with
 196 an easterly and north easterly direction. Polluted aerosols were transported along with the wind to the
 197 west and south of the study area. They accumulated in the downstream area, resulting in a high value of
 198 AOD. On September 1st, 3rd, and 4th September, the GBA was in an the area of low wind speed, which
 199 was not conducive to the regional transport of particulate matter. As a result, the AOD value of the
 200 whole GBA reached a higher level, of which the increase in of AOD in the northern region was more
 201 obvious. AOD values on these days distributed more homogeneously than days with higher wind speed.
 202 On 2-September 2nd, the lower winds of the GBA turned westerly when the observation area in the east
 203 was downstream, and the highest points of the AOD value also appeared on the eastern route. Such
 204 results show that the horizontal distribution of particles in the GBA was closely related to wind speed
 205 and wind direction.



207
 208 **Figure 23.** (a)-(g) Aerosol optical depth (AOD) measured at 532 nm with the MPL in the route from 29 August
 209 29th to 4 September 4th, 2020, and (h) Guangdong–Hong Kong–Macao Greater Bay Area and route details
 210 of the route.





213

214

215

216 **Figure 34.** (a)-(g) Wind field of 925 hPa from 29 August 29th to 4 September 4th, 2020 from ERA5 reanalysis
 217 data. The colour map represents horizontal wind speed (m/s). Red arrows represent the wind direction. The

218 orange box shows the location of the GBA area.

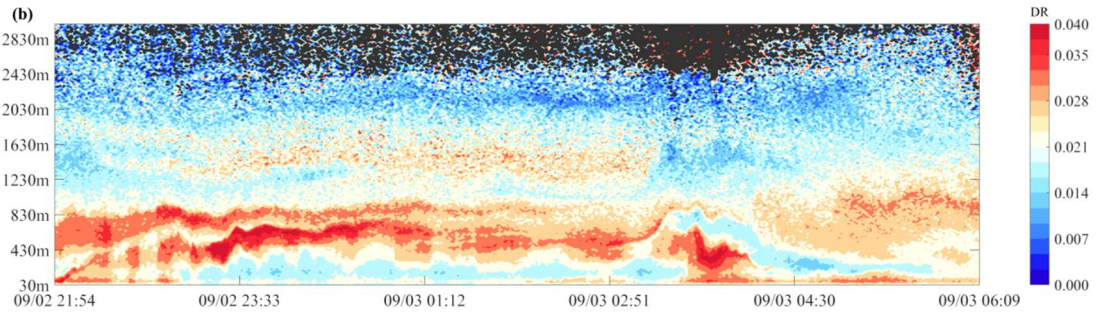
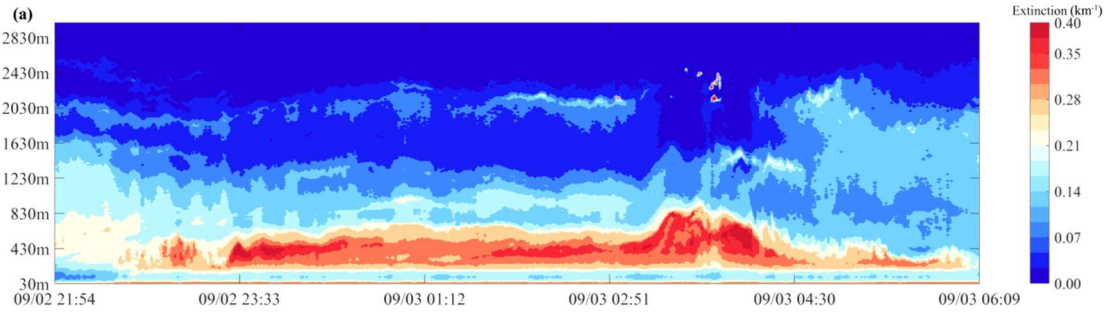
219

220 **3.2 In-SituFixed-location –Lidar Observations**

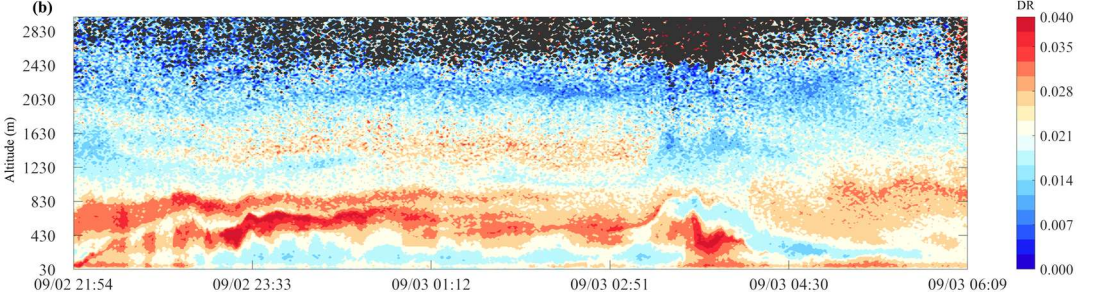
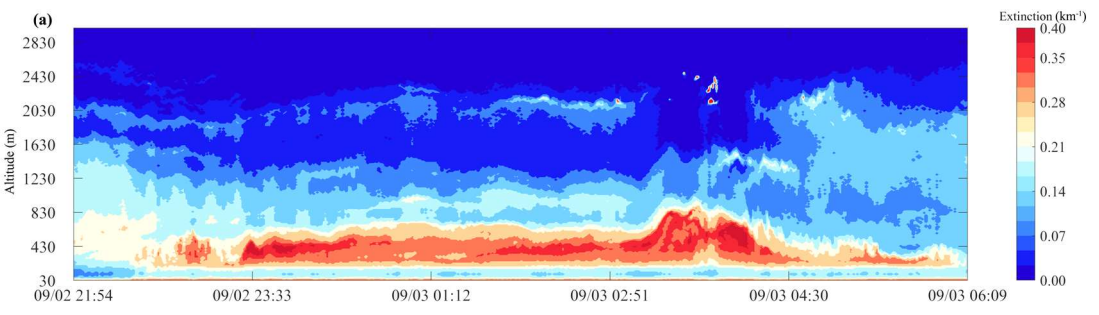
221 To obtain the vertical distribution of particles, fixed-location in-situ lidar observations were conducted
222 at the Haizhu Lake Research Base, which is located in the centre of the metropolis in Guangzhou,
~~which could typically represent the situation of the GBA. As daytime temperatures in the GBA were~~
~~still high in September and October, the development of the convective boundary layer during the day~~
~~was vigorous, making it conducive to particle diffusion. Therefore, the value of the extinction~~
~~coefficient near the ground during the day was generally low. The hierarchical structure of aerosols~~
~~occurred more frequently at night. The research base is representative of the distribution of urban~~
~~aerosols. Unfortunately, there is no remote sensing device in the base. This motivated us to park the car~~
~~in the base and conduct a total of 89 days of fixed-location observation. During this period, we found~~
~~that the hierarchical structure of aerosols occurred more frequently at night, and most of the vertical~~
~~aerosol distributions are consistent with three distribution types. Therefore, we selected the three most~~
~~representative processes for analysing the three distribution types.~~ Three different vertical distribution
233 types of particles are given below, as well as the corresponding vertical observation results of
234 temperature and wind in the same period. Altitude values in the following figures refer to the altitude
235 above instrument.

236 **3.2.1 Type I: Surface Single Layer**

237 On 3 September 3rd, 2020, a clear night in autumn, the lidar system operated from 2154 to 0609 local
238 time (LT) the next day. Figure 45(a) shows the time series of the extinction coefficient of a single
239 aerosol layer on the surface, which was observed with the MPL. Before 0300 LT, particles accumulated
240 below 800 m. The maximum value of the extinction coefficient near the ground was between 0.3–0.5.
241 During 0300 LT and 0400 LT, there is a significant increase in the maximum height of the particle
242 layer. After 0430 LT, the maximum height of the particle layer dropped, and the near-ground extinction
243 coefficient fell below 0.3. Figure 45(b) shows the time series of corresponding depolarization ratio
244 profiles. Most of the depolarization ratios were below 0.1, consistent with previous research on the
245 GBA (Tian et al., 2017). A layer of elevated depolarization ratio was visible near the boundary of the
246 surface single layer in Figure 35(ab). It can be seen that during 0300 LT and 0400 LT, there was a
247 significant hierarchical structure with a high depolarization ratio layer near the ground and another
248 layer of high value above. A layer with a lower value of depolarization ratio existed between the two
249 layers with a higher value. This result indicated that there might be local anthropogenic emissions
250 during the period.



251



252

253 **Figure 45.** Extinction coefficient at 532 nm (a) and depolarization ratio (b) at 532 nm from 2154 LT-02 on
254 September 2nd, 2020, to 0609 LT on-03 September 3rd, 2020.

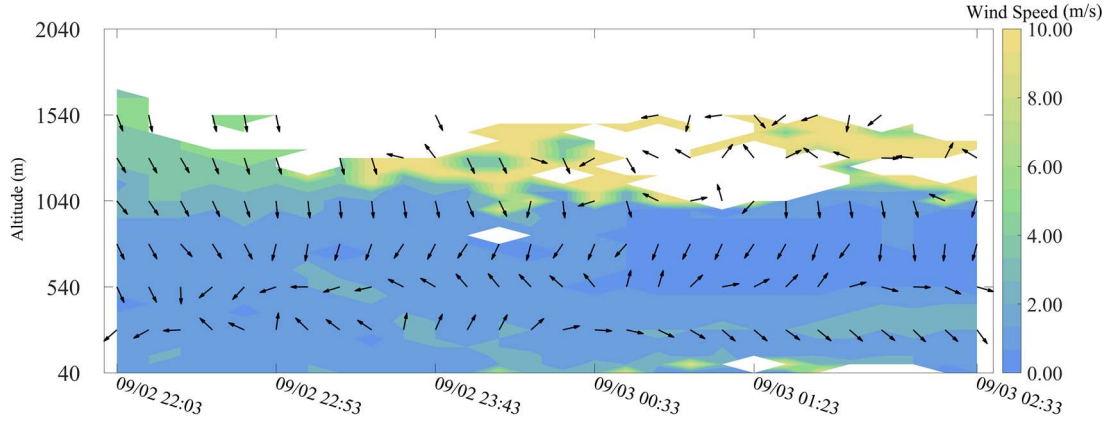
255

256 Figure 5-6 shows the horizontal wind speed and wind direction over the observation points of the fixed-
257 location observation in this period. Noticeably, a light wind layer appeared below 1000 m, with
258 horizontal wind speeds of each height maintained below 2 m/s. Such a static and stable condition was
259 advantageous to the accumulation of locally generated particulate matter near the ground. However,
260 light wind at higher altitude (500–1000 m) it acted as a disincentive to prevent the regional transport
261 of particulate matter at a higher altitude, because it is difficult for such a low wind speed to blow the
262 particulate matter at the corresponding height to the downstream area. Therefore, when calm-light wind
263 dominated near the ground, the particulate matter was likely to form a single layer on the surface.

264

265 It is worth noting that the wind at an altitude of 540 m at night gradually shifted to southerly wind,
266 ~~while whereas~~ the northerly weight of the 290 m altitude wind gradually increased. This shift in the
267 wind was typical of a sea-land breeze in nocturnal coastal areas, which can only be observed when the
268 background wind speed was relatively low.

269

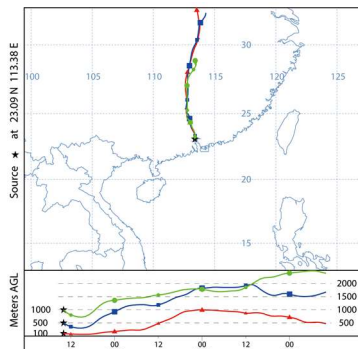


270
271 **Figure 56.** Wind speed and wind direction of Type I. The colour map represents horizontal wind speed (m/s).
272 Arrows represents the wind direction.

273

274 The backward trajectories analysis of the same period (Figure 67) shows that on a large scale, the
275 airflow in the boundary layer came from the north. The vertical trajectories of each layer were roughly
276 parallel within 24 h, and all ~~traveled moved~~ from high altitude to low, suggesting that particulate matter
277 emitted near the ground in neighbouring cities was not easily transported by wind to Guangzhou.

278

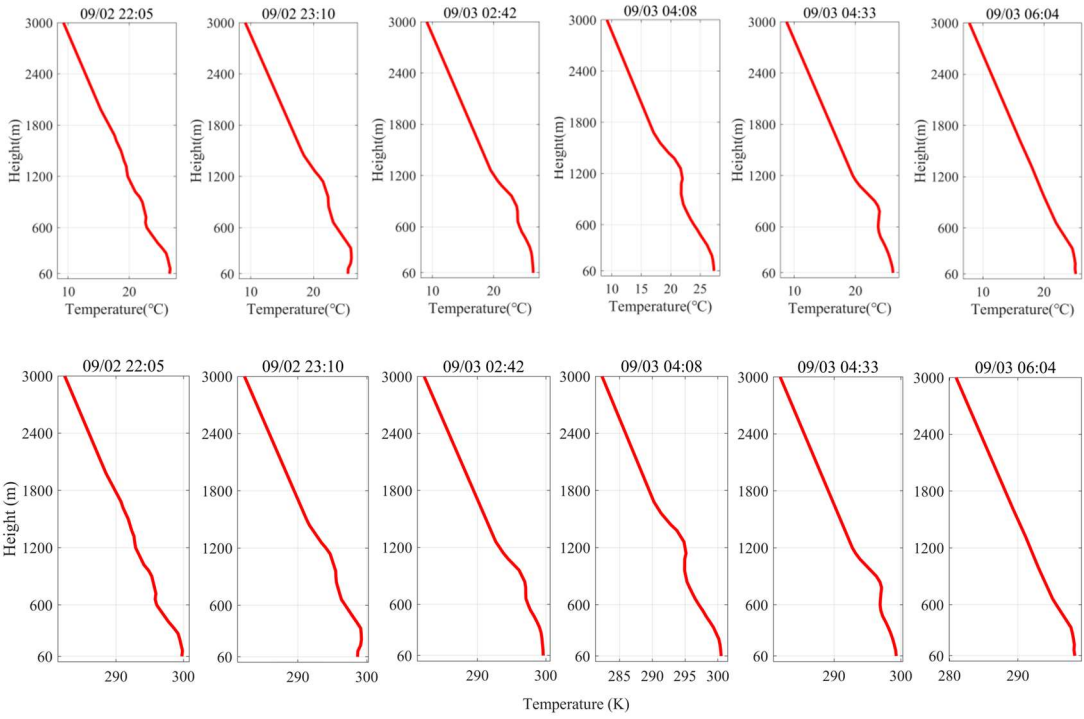


279
280 **Figure 67.** Backward trajectories at 100 m, 500 m, and 1000 m, ending at 2200 LT 02-September 2020,
281 determined by the HYSPLIT model.

282

283 Observations from the Raman temperature profile lidar (Figure 78) show an inversion between 600–
284 1200 m before 0300 LT, which then rose to 1200 m and shrank to near the ground. Temperature
285 inversion often exists at the top of the planetary boundary layer, trapping moisture and aerosols (Seibert
286 et al., 2000). Hence, changes in the height of the inversion coincided with the trend of the top of the
287 particulate matter layer on the vertical dimension revealed by MPL.

288



289

290

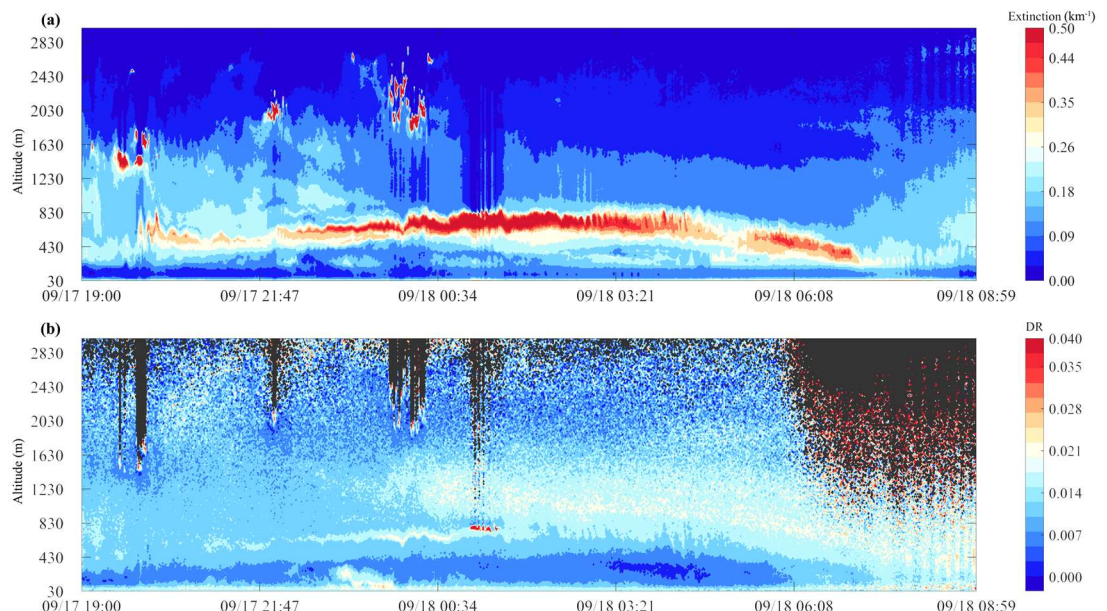
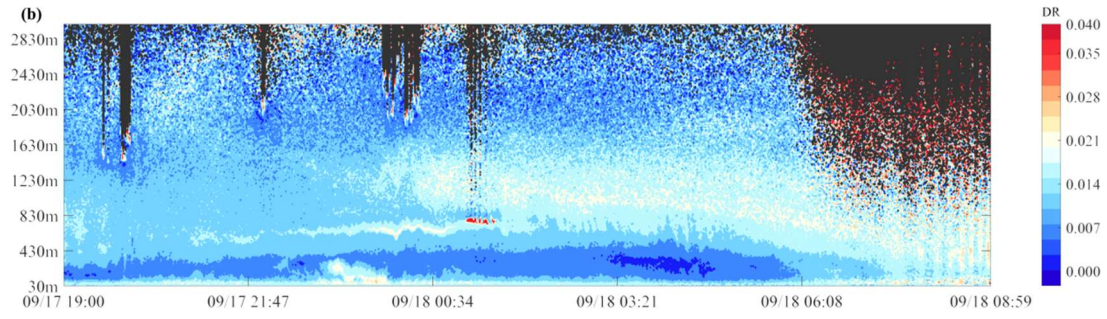
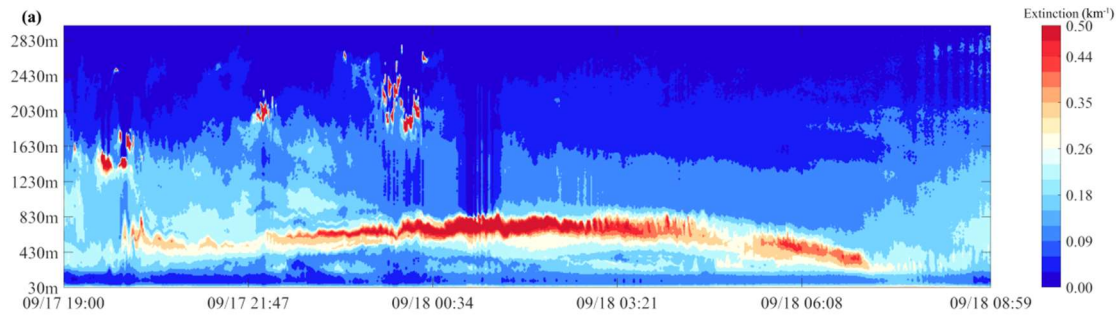
291

292

Figure 78. Temperature profiles from the evening of 2 September 2nd, 2020 to the early hours of 3 September 3rd, 2020.

293 3.2.2 Type II: Elevated Single Layer

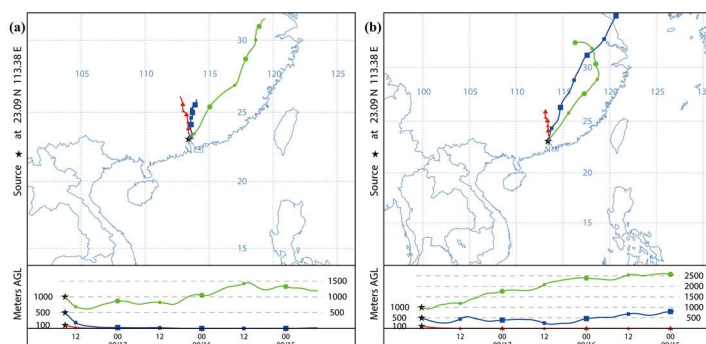
294 The particle layer was not only distributed near the ground but sometimes suspended at a higher
 295 altitude in the air. Figure 89(a) shows the extinction coefficient time series of an elevated single layer of
 296 particulate matter. The low extinction coefficient near the ground suggests that it was clean below 400
 297 m during in the nighttime. The height of the high extinction coefficient layer gradually rose from 500–
 298 800 m at night, which then dropped below 400 m after dawn. The high value of the extinction
 299 coefficient corresponded to a higher depolarization ratio than the lower layer, which was approximately
 300 0.02. However, the depolarization ratio of **Type II** was significantly lower than the depolarization ratio
 301 of the particle layer near the surface of **Type I**. This differing depolarization ratio was because local
 302 emissions dominated in **Type I**, and the primary pollutant emissions from anthropogenic sources near
 303 the surface with a non-spherical character and larger particle sizeunconverted primary particulate
 304 matter with larger particle size accounted for a larger amount than that of **Type II**.
 305



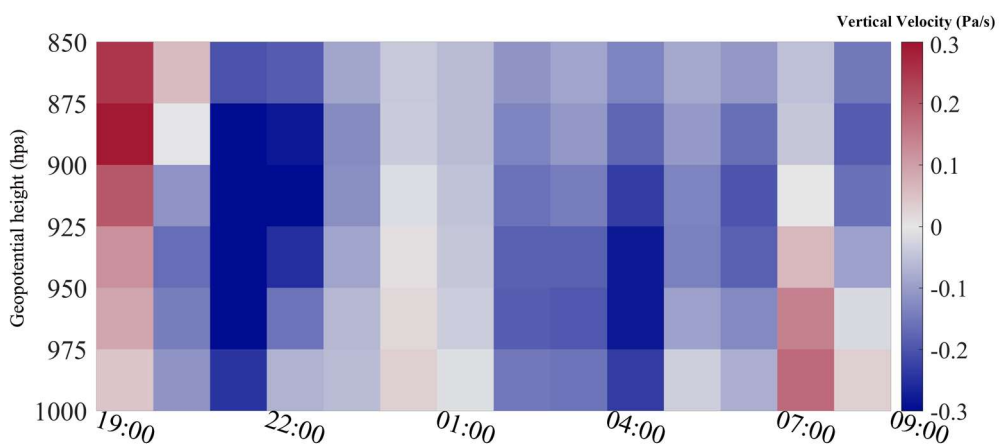
308 **Figure 89.** Extinction coefficient at 532 nm (a) and depolarization ratio (b) at 532 nm from 1900 LT 17 on
309 September 17th, 2019 to 0859 LT on 18 September 18th, 2019.

310
311 Figure 910(a) indicated that backward trajectories at 500 m and 100 m were both from near the ground,
312 elevating particles from lower levels vertically. Meanwhile, lower trajectories also carried particles
313 from the upper reaches of the region over Guangzhou horizontally. Wind speed at lower altitudes was
314 relatively low, which was beneficial to regional transport. The domination of weak wind in the
315 boundary layer was beneficial to inter-city transport of particles. It brought particles from cities located
316 upstream to the location of our observation and allowed particles to stay longer without being blown
317 quickly downstream. In contrast, the trajectory at 1000 m came from a distance in the Yangtze River
318 Delta with a larger wind speed, and the trajectory remained at a high altitude. Particles at 1000 m
319 cannot stay for a long time and were quickly transported downstream by strong winds. Hence, upward

320 airflow near the ground and vertical wind shear at a higher altitude were the causes of particulate
 321 matter forming an elevated single layer. Unfortunately, the temperature profile and wind profile data
 322 were missing owing to sampling failures. This upward convection of particles was confirmed by the
 323 ERA5 vertical velocity reanalysis data of the corresponding time, shown in Figure 4011.
 324



325
 326 **Figure 109.** Backward trajectories at 100 m, 500 m, and 1000 m, ending at 2300 LT **17** September **17th**, 2019
 327 (a) and 0700 LT **18** September **18th**, 2019 (b), determined by the HYSPLIT model.

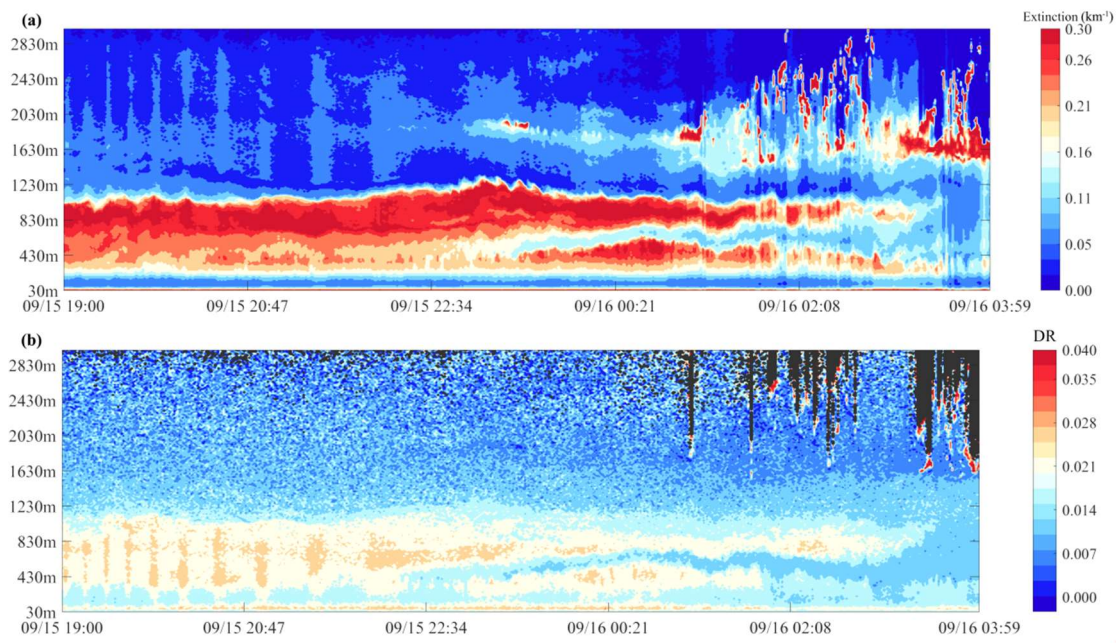


331
 332 **Figure 1011.** ERA5 hourly vertical velocity from 1900 LT **17** on September **17th**, 2019, to 0900 LT on **18**
 333 September **18th**, 2019, at 23.25°N, 113.25°E. Negative values indicate upward motion.

336 3.2.3 Type III: Double Layer

337 Figure 11–12 presents a thick single layer of particles transforming into a double layer structure. There
 338 was a layer concentrated near the ground after 2300 LT, along with another layer suspended at the
 339 height of 600–1000 m. A cleaner layer with a lower extinction coefficient existed between the two
 340 particle layers. The depolarization ratio of the suspending layer was higher than the layer near the
 341 surface, especially after 0100 LT, which indicated that sources of the two layers might be different.
 342

343



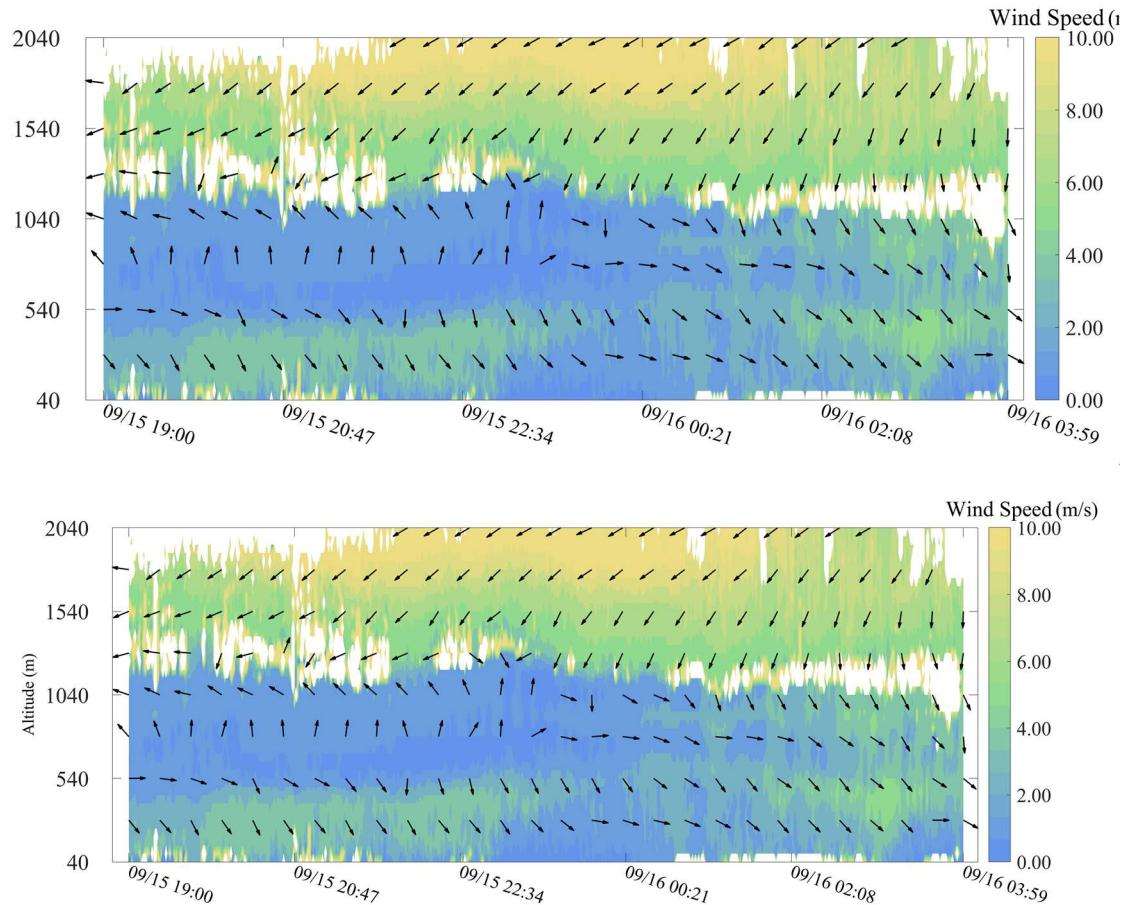
344

345 **Figure 4112.** Extinction coefficient at 532 nm (a) and depolarization ratio (b) at 532 nm from 1900 LT 15 on
 346 September 15th, 2019 to 0359 LT on 16 September 16th, 2019.

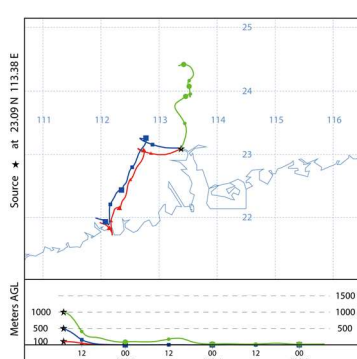
347

348 The vertical distribution of particulate matter was closely related to the horizontal wind speed at
 349 various heights (Figure 4213). It can be seen that the wind speed of more than 1000 m increased
 350 significantly with the altitude, reaching more than 6 m/s. By 2300 LT, the wind speed below 500 m was
 351 approximately 4 m/s, obviously higher than the wind speed between 500–1000 m, and there were
 352 significant differences in the wind direction. After 2300 LT, the wind speed near the ground decreased,
 353 and wind direction gradually turned consistent with the upper level. The wind speed at 500 m
 354 continued to be high, reaching 6 m/s maximum. The layer with higher wind speed corresponded to
 355 the height of the cleaner layer, which facilitated the transport of particulate matter downstream in a
 356 horizontal direction. Figure 43–14 illustrates the backward trajectories when the double layer appeared.

357 As shown in Figure 1314, the layer of particulate matter below 500 m may have originated in the
 358 southwest of the GBA²⁵ whereas, the layer of particulate matter at 1000 m may have originated in the
 359 Qingyuan and Shaoguan of northern Guangdong from cities north of the GBA area.



360
 361
 362 Figure 4213. Wind speed and wind direction of Type III.
 363

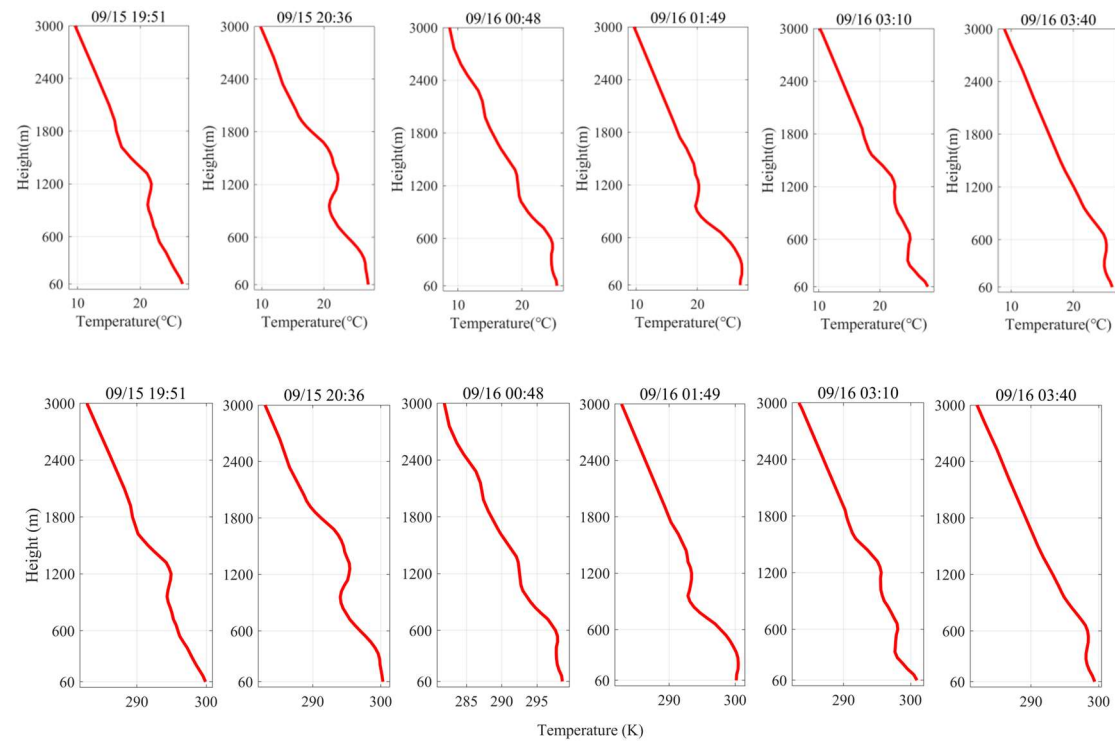


364
 365 Figure 4314. Backward trajectories at 100 m, 500 m, and 1000 m, ending at 0100 LT 16 September 16th, 2019,
 366 determined by the HYSPLIT model.

367
 368 The vertical observations of the temperature (Fig. 4415.) showed that on the night of 15th September
 369 2019, there was an inversion at 1200 m, which grew thicker. At 0048 LT, like the distribution of
 370 the extinction coefficient, the inversion transformed into a double layer structure, with one remaining at
 371 1200 m and another existing under 600 m. The vertical distributed double inversion, which allowed

372 particulate matter to concentrate at the corresponding height, resulted in a double layer distribution of
373 particulate matter.

374



375

376

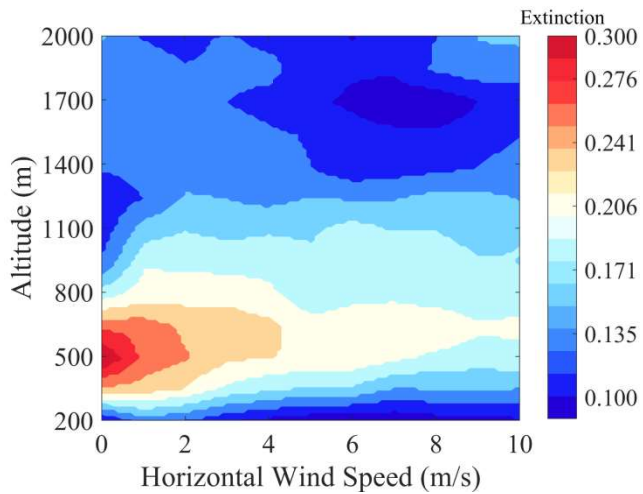
377 **Figure 1415.** Temperature profiles from the evening of 15 September 15th, 2019 to the early hours of 16
378 September 16th, 2019.

379

380 3.3 Effect of Meteorological Elements on the Distribution of Particles

381 3.3.1 Extinction Coefficient at Different Wind Speeds

382 Using data of in situ observations during September and October of 2019 and 2020, statistics of
383 average extinction coefficients at different altitudes and horizontal wind speeds were gathered, as
384 shown in Figure 1516. To eliminate the influence of clouds on the extinction coefficient, observations
385 during cloudy weather were manually screened out based on the original signal of the MPL output and
386 images of the sky above the field taken automatically by a camera. Because the spatial resolutions of
387 the data from the two lidar are different, we interpolated the data to make them match each other
388 vertically. The result shows that 500 m was the height with the highest average extinction coefficient,
389 which indicated that the particle layer was most likely to appear at this height. The horizontal wind
390 speed had different effects on the lower and upper parts of the boundary layer. Below 800 m, the
391 extinction coefficient decreased as the wind speed increased, but it was the opposite above 800 m; i.e.,
392 the extinction coefficient increased with the wind speed. This altering of the extinction coefficient was
393 because most of the particulate matter in the lower layer came from local emissions and easily
394 accumulated in the presence of a layer with calm wind near the ground. However, in the upper layer,
395 particulate matter was derived more from the surrounding areas, necessitating a certain minimum
396 horizontal wind speed before it could be transported by the wind.



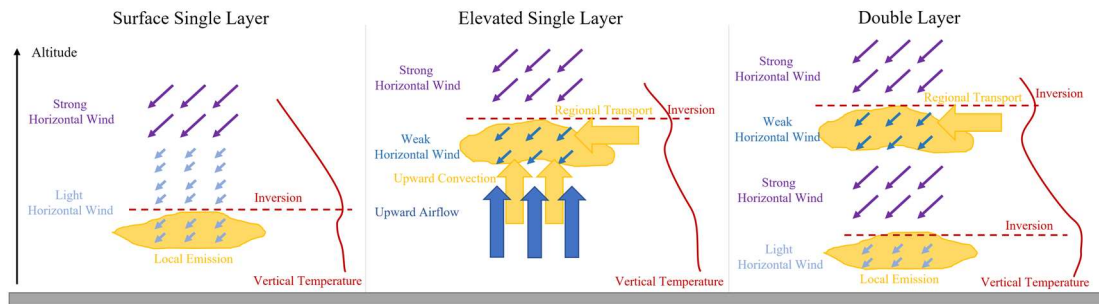
398
 399 **Figure 4516.** Average extinction coefficient at different wind speeds and altitude from fixed-location
 400 observations of a total of 89 days at Haizhu Lake Research Base, during September and October of 2019 and
 401 2020.
 402

403 3.3.2 Conceptual Model of Meteorological Elements and Vertical Distribution of Particles

404 Based on the observational research above, a conceptual model was developed to summarize
 405 summarise the effect of meteorological elements on the three typical vertical distributions of particles
 406 in the GBA.

407
 408 As shown in Figure 4617, the surface single layer occurred when calm light horizontal wind dominated
 409 near the ground, which was not conducive to removing particles from local emissions. An elevated
 410 single layer was caused by upward airflow near the ground and vertical wind shear at a higher altitude.
 411 In this kind of wind structure, particle layer formation was dominated by upward convection and
 412 regional transport. A double layer existed because a layer with stronger horizontal wind existed
 413 between two layers with weaker wind, which facilitated the transport of particles from local emission
 414 and horizontal transport to downstream areas and resulted in a cleaner layer inside the polluted air
 415 mass.

416
 417 Another key factor that influenced the vertical distribution of particles was temperature inversion,
 418 which trapped most anthropogenic emissions from the surface, preventing them from penetrating out of
 419 the boundary layer. Furthermore, multiple inversions can cause more than one peak in the
 420 concentration of particles vertically.



422

423 **Figure 1617. Conceptual model of meteorological elements and vertical distribution of particles.**

424

425 4. Conclusion

426 ~~Vehicle based and in situ multi lidar observations were conducted during September and October of 2019 and 2020 to study the horizontal and vertical distribution of particles in the GBA. The temperature and wind profiles in the boundary layer were analyzed and confirmed to have a crucial impact on particle distribution characteristics.~~

430

431 ~~The horizontal distribution of particles in the GBA was closely related to wind speed and wind direction. On days with stronger wind in the boundary layer, high values of AOD were mostly distributed in the downstream areas. On days with weaker wind, the horizontal distribution of particles in the GBA presented homogeneously.~~

435

436 ~~The vertical distribution of particles in the GBA was classified into three typical types according to the observations of the MPL: surface single layer, elevated single layer, and double layer. The result of the Doppler wind profile lidar and HYSPLIT backward trajectory model suggested that the sources of the particulate matter of the three types differed. The surface single layer occurred when wind with low speed dominated the boundary layer. The elevated single layer was caused by upward airflow near the ground and vertical wind shear at a higher altitude. The double layer existed because a layer with higher horizontal wind speed existed between two layers with weaker wind. Particles were concentrated near the temperature inversion. Multiple inversions can cause more than one peak in the concentration of particulate matter vertically.~~

445

446 ~~The statistics of average extinction coefficients at different altitudes and horizontal wind speeds revealed the following two mechanisms that affected the distribution of particulate matter in the upper and lower boundary layers. Lower horizontal wind speed was conducive to accumulating particulate matter near the ground. In contrast, higher horizontal wind speed promoted the transport of particles between surrounding areas in the upper boundary layer.~~

447 ~~The results of our study show how meteorological elements affected the three-dimensional distribution of particles in the western Guangdong–Hong Kong–Macao Greater Bay area. We focused mainly on the periods when the wet season changes to the dry season, as the frequently changing temperature and wind under such conditions have a more significant impact on the distribution of particles. The horizontal distribution of particles in the GBA was closely related to wind speed and wind direction.~~

456 On days with stronger winds in the boundary layer, high values of AOD were mostly distributed in the
457 downstream areas. On days with weaker winds, the horizontal distribution of particles in the GBA was
458 homogeneous. The vertical distribution of particles in the GBA was classified into three typical types:
459 surface single layer, elevated single layer, and double layer. The surface single layer occurred when
460 wind with very low speed dominated the boundary layer. The elevated single layer was caused by
461 upward airflow near the ground and vertical wind shear at a higher altitude. The double layer existed
462 because a layer with higher horizontal wind speed existed between two layers with weaker wind.
463 Particles were concentrated near the temperature inversion. Multiple inversions can cause more than
464 one peak in the vertical distribution of particulate matter. The mechanisms that affected the distribution
465 of particulate matter in the upper and lower boundary layers are different. Lower horizontal wind speed
466 was conducive to accumulating particulate matter near the ground, whereas higher horizontal wind
467 speed promoted the transport of particles between surrounding areas in the upper boundary layer.

468
469 Further studies should be conducted ~~to carry out observations~~ during other seasons in the western
470 Guangdong–Hong Kong–Macao Greater Bay Area to further verify the conceptual model of
471 meteorological elements and vertical distribution of particles proposed in this article. In addition, more
472 vertical observation instruments for meteorological elements, such as a radiometer, could be added to
473 the multi-lidar system to further study the influence of the three-dimensional distribution of humidity,
474 air pressure, and other meteorological elements on the distribution of particles.

475 **Acknowledgments**

476 This work was supported by the National Natural Science Foundation of China (Grant No. 41630422)
477 and the Guangdong Major Project of Basic and Applied Basic Research (Grant No.
478 2020B0301030004).

481 **References**

482
483 Dai, G., Wu, S., and Song, X.: Depolarization ratio profiles calibration and observations of aerosol
484 and cloud in the Tibetan Plateau based on polarization Raman lidar, Remote Sensing, 10(3), 378,
485 <https://doi.org/10.3390/rs10030378>, 2018.

486
487 Deng, T., Deng, X., Li, F., Wang, S., and Wang, G.: Study on aerosol optical properties and
488 radiative effect in cloudy weather in the Guangzhou region, Science of the Total Environment,
489 568, 147–154, <https://doi.org/10.1016/j.scitotenv.2016.05.156>, 2016.

490
491 Du, W., Zhang, Y., Chen, Y., Xu, L., Chen, J., Deng, J., Hong, Y., and Xiao, H.: Chemical
492 characterization and source apportionment of PM2. 5 during spring and winter in the Yangtze
493 River Delta, China, Aerosol and Air Quality Research, 17, 2165–2180,
494 <https://doi.org/10.4209/aaqr.2017.03.0108>, 2017.

495
496 Fan, S., Liu, C., Xie, Z., Dong, Y., Hu, Q., Fan, G., Chen, Z., Zhang, T., Duan, J., Zhang, P., and
497 Liu, J.: Scanning vertical distributions of typical aerosols along the Yangtze River using elastic
498 lidar, Science of The Total Environment, 628, 631-641,
499 <https://doi.org/10.1016/j.scitotenv.2018.02.099>, 2018.

500
501 Fang, X., Fan, Q., Li, H., Liao, Z., Xie, J., and Fan, S.: Multi-scale correlations between air quality
502 and meteorology in the Guangdong–Hong Kong–Macau Greater Bay Area of China during 2015–
503 2017, *Atmospheric Environment*, 191, 463–477, <https://doi.org/10.1016/j.atmosenv.2018.08.018>,
504 2018.

505
506 Fang, X., Fan, Q., Liao, Z., Xie, J., Xu, X., & Fan, S.: Spatial-temporal characteristics of the air
507 quality in the Guangdong–Hong Kong–Macau Greater Bay Area of China during 2015–2017,
508 *Atmospheric Environment*, 210, 14–34, <https://doi.org/10.1016/j.atmosenv.2019.04.037>, 2019.

509
510 Fernald, F. G.: Analysis of atmospheric lidar observations: some comments, *Applied optics*, 23,
511 652–653, 1984.

512
513 He, Y., Wang, H., Wang, H., Xu, X., Li, Y., & Fan, S.: Meteorology and topographic influences on
514 nocturnal ozone increase during the summertime over Shaoguan, China, *Atmospheric*
515 Environment, 256, 118459, <https://doi.org/10.1016/j.atmosenv.2021.118459>, 2021b.

516
517 He, Y., Xu, X., Gu, Z., Chen, X., Li, Y., and Fan, S.: Vertical distribution characteristics of aerosol
518 particles over the Guanzhong Plain, *Atmospheric Environment*, 255, 118444,
519 <https://doi.org/10.1016/j.atmosenv.2021.118444>, 2021a.

520
521 Heese, B., Baars, H., Bohlmann, S., Althausen, D., and Deng, R.: Continuous vertical aerosol
522 profiling with a multi-wavelength Raman polarization lidar over the Pearl River Delta, China,
523 *Atmos. Chem. Phys.*, 17, 6679–6691, <https://doi.org/10.5194/acp-17-6679-2017>, 2017.

524
525 Huang T., Li Y., Cheng J.C.H., Haywood J., Hon K.K., Lam D.H.Y., Lee O.S.M., Lolli S.,
526 O'Connor E.J., Lee H.F., Wang M., and Yim S.H.L.: Assessing Transboundary-local Aerosols
527 Interaction over Complex Terrain Using a Doppler LiDAR Network, *Geophysical Research*
528 Letters, 48, 12, <https://doi.org/10.1029/2021GL093238>, 2021a.

529
530 Huang, T., Yang, Y., O'Connor, E. J., Lolli, S., Haywood, J., Osborne, M., Cheng, J. C. H. C.,
531 Guo, J., and Yim, S. H. L.: Influence of a weak typhoon on the vertical distribution of air pollution
532 in Hong Kong: A perspective from a Doppler LiDAR network, *Environmental Pollution*, 276,
533 <https://doi.org/10.1016/j.envpol.2021.116534>, 2021b.

534
535 Huige, D., Siwen, L., Yun, Y., and Dengxin, H.: Observational study of the vertical aerosol and
536 meteorological factor distributions with respect to particulate pollution in Xi'an, *Atmospheric*
537 Environment, 247, 118215, <https://doi.org/10.1016/j.atmosenv.2021.118215>, 2021.

538
539 Leikauf, G. D., Kim, S. H., and Jang, A. S.: Mechanisms of ultrafine particle-induced respiratory
540 health effects, *Experimental & Molecular Medicine*, 52, 329–337, <https://doi.org/10.1038/s12276-020-0394-0>, 2020.

542
543 Li, Y., Wang, B., Lee, S. Y., Zhang, Z., Wang, Y., and Dong, W.: Micro-Pulse Lidar Cruising

544 Measurements in Northern South China Sea, *Remote Sensing*, 12, 1695,
545 <https://doi.org/10.3390/rs12101695>, 2020.

546

547 Liao, Z., Gao, M., Sun, J., and Fan, S.: The impact of synoptic circulation on air quality and
548 pollution-related human health in the Yangtze River Delta region, *Science of the Total
549 Environment*, 607, 838–846, <https://doi.org/10.1016/j.scitotenv.2017.07.031>, 2017.

550

551 Liu, J., Wu, D., Fan, S., Mao, X., and Chen, H.: A one-year, on-line, multi-site observational study
552 on water-soluble inorganic ions in PM_{2.5} over the Pearl River Delta region, China, *Science of the
553 Total Environment*, 601, 1720–1732, <https://doi.org/10.1016/j.scitotenv.2017.06.039>, 2017.

554

555 Liu, Q., He, Q., Fang, S., Guang, Y., Ma, C., Chen, Y., Kang, Y., Pan, H., Zhang, H., and Yao, Y.:
556 Vertical distribution of ambient aerosol extintive properties during haze and haze-free periods
557 based on the Micro-Pulse Lidar observation in Shanghai, *Science of the Total Environment*, 574,
558 1502–1511, <https://doi.org/10.1016/j.scitotenv.2016.08.152>, 2017.

559

560 Lu, X., Mao, F., Pan, Z., Gong, W., Wang, W., Tian, L., and Fang, S.: Three-dimensional physical
561 and optical characteristics of aerosols over central china from long-term CALIPSO and HYSPLIT
562 data, *Remote Sensing*, 10, 314, <https://doi.org/10.3390/rs10020314>, 2018.

563

564 Lv, L., Liu, W., Zhang, T., Chen, Z., Dong, Y., Fan, G., Xiang, Y., Yao, Y., Yang, N., Chu, B.,
565 Teng, M., and Shu, X.: Observations of particle extinction, PM_{2.5} mass concentration profile and
566 flux in north China based on mobile lidar technique. *Atmospheric Environment*, 164, 360–369,
567 <https://doi.org/10.1016/j.atmosenv.2017.06.022>, 2017.

568

569 [Lv, L., Xiang, Y., Zhang, T., Chai, W., and Liu, W.: Comprehensive study of regional haze in the
570 North China Plain with synergistic measurement from multiple mobile vehicle-based lidars and a
571 lidar network, *Science of the Total Environment*, 721, 137773,
572 https://doi.org/10.1016/j.scitotenv.2020.137773, 2020.](#)

573

574 Lyu, L., Dong, Y., Zhang, T., Liu, C., Liu, W., Xie, Z., Xiang, Y., Zhang, Y., Chen, Z., Fan, G.,
575 Zhang, L., Liu, Y., Shi, Y., and Shu, X.: Vertical Distribution Characteristics of PM_{2.5} Observed by
576 a Mobile Vehicle Lidar in Tianjin, China in 2016, *Journal of Meteorological Research*, 32, 60–68,
577 <https://doi.org/10.1007/s13351-018-7068-z>, 2018.

578

579 Kim, H. C., Chai, T., Stein, A., and Kondragunta, S.: Inverse modeling of fire emissions
580 constrained by smoke plume transport using HYSPLIT dispersion model and geostationary
581 satellite observations, *Atmos. Chem. Phys.*, 20, 10259–10277, <https://doi.org/10.5194/acp-20-10259-2020>, 2020.

583

584 Orru, H., Ebi, K. L., and Forsberg, B.: The interplay of climate change and air pollution on health,
585 Current environmental health reports, 4, 504–513, <https://doi.org/10.1007/s40572-017-0168-6>,
586 2017.

587

588 Seibert, P., Beyrich, F., Gryning, S. E., Joffre, S., Rasmussen, A., and Tercier, P.: Review and
589 intercomparison of operational methods for the determination of the mixing height, *Atmospheric*
590 *Environment*, 34, 1001–1027, [https://doi.org/10.1016/S1352-2310\(99\)00349-0](https://doi.org/10.1016/S1352-2310(99)00349-0), 2000.

591

592 Sekuła, P., Bokwa, A., Bartyzel, J., Bochenek, B., Chmura, Ł., Gałkowski, M., and Zimnoch, M.:
593 Measurement report: Effect of wind shear on PM₁₀ concentration vertical structure in the urban
594 boundary layer in a complex terrain, *Atmos. Chem. Phys.*, 21, 12113 – 12139,
595 <https://doi.org/10.5194/acp-21-12113-2021>, 2021.

596

597 Shao, Q., Liu, X., and Zhao, W.: An alternative method for analyzing dimensional interactions of
598 urban carrying capacity: case study of Guangdong–Hong Kong–Macao Greater Bay Area, *Journal*
599 *of Environmental Management*, 273, 111064, <https://doi.org/10.1016/j.jenvman.2020.111064>,
600 2020.

601

602 Stocker, T. (Ed.): *Climate change 2013: the physical science basis: Working Group I contribution*
603 *to the Fifth assessment report of the Intergovernmental Panel on Climate Change*, Cambridge
604 university press, 2014.

605

606 Strawa, A. W., Kirchstetter, T. W., Hallar, A. G., Ban-Weiss, G. A., McLaughlin, J. P., Harley, R.
607 A., and Lunden, M. M.: Optical and physical properties of primary on-road vehicle particle
608 emissions and their implications for climate change, *Journal of Aerosol Science*, 41, 36–50,
609 <https://doi.org/10.1016/j.jaerosci.2009.08.010>, 2010.

610

611 Tian, P., Cao, X., Zhang, L., Sun, N., Sun, L., Logan, T., Shi, J., Wang, Y., Ji, Y., Lin, Y., Huang,
612 Z., Zhou, T., Shi, Y., and Zhang, R.: Aerosol vertical distribution and optical properties over China
613 from long-term satellite and ground-based remote sensing, *Atmos. Chem. Phys.*, 17, 2509–2523,
614 <https://doi.org/10.5194/acp-17-2509-2017>, 2017.

615

616 Wallace, J., and Kanaroglou, P.: The effect of temperature inversions on ground-level nitrogen
617 dioxide (NO₂) and fine particulate matter (PM_{2.5}) using temperature profiles from the
618 Atmospheric Infrared Sounder (AIRS), *Science of the Total Environment*, 407, 5085–5095,
619 <https://doi.org/10.1016/j.scitotenv.2009.05.050>, 2009.

620

621 Wang, H., Sun, Z., Li, H., Gao, Y., Wu, J., and Cheng, T: Vertical-distribution characteristics of
622 atmospheric aerosols under different thermodynamic conditions in Beijing, *Aerosol and Air*
623 *Quality Research*, 18(11), 2775-2787, <https://doi.org/10.4209/aaqr.2018.03.0078>, 2018.

624

625 Xie, J., Liao, Z., Fang, X., Xu, X., Wang, Y., Zhang, Y., Liu, J., Fan, S., and Wang, B.: The
626 characteristics of hourly wind field and its impacts on air quality in the Pearl River Delta region
627 during 2013–2017, *Atmospheric Research*, 227, 112–124,
628 <https://doi.org/10.1016/j.atmosres.2019.04.023>, 2019.

629

630 Xu, Y., Xue, W., Lei, Y., Zhao, Y., Cheng, S., Ren, Z., and Huang, Q.: Impact of meteorological
631 conditions on PM_{2.5} Pollution in China during winter, *Atmosphere*, 9, 429,

632 <https://doi.org/10.3390/atmos9110429>, 2018.

633

634 Yao, L., Zhan, B., Xian, A., Sun, W., Li, Q., and Chen, J.: Contribution of transregional transport
635 to particle pollution and health effects in Shanghai during 2013–2017, *Science of the Total
636 Environment*, 677, 564-570, <https://doi.org/10.1016/j.scitotenv.2019.03.488>, 2019.s
637

638 Zang, Z., Wang, W., You, W., Li, Y., Ye, F., and Wang, C.: Estimating ground-level PM_{2.5}
639 concentrations in Beijing, China using aerosol optical depth and parameters of the temperature
640 inversion layer, *Science of the Total Environment*, 575, 1219–1227,
641 <https://doi.org/10.1016/j.scitotenv.2016.09.186>, 2017.

642

643 [Zhao, Y. F., Gao, J., Cai, Y. J., Wang, J. J., and Pan, J.: Real-time tracing VOCs, O₃ and PM_{2.5}
644 emission sources with vehicle-mounted proton transfer reaction mass spectrometry combined
645 differential absorption lidar, *Atmospheric Pollution Research*, 12\(3\), 146-153,
646 <https://doi.org/10.1016/j.apr.2021.01.008>, 2021.](https://doi.org/10.1016/j.apr.2021.01.008)

647

648 Zhou, Y., Shan, Y., Liu, G., and Guan, D.: Emissions and low-carbon development in Guangdong-
649 Hong Kong-Macao Greater Bay Area cities and their surroundings, *Applied energy*, 228,
650 1683–1692, <https://doi.org/10.1016/j.apenergy.2018.07.038>, 2018.

651

652